

Impulsively started flow separation in wavy-walled tubes

By FEDERICO DOMENICHINI AND GIANNI PEDRIZZETTI

Dipartimento Ingegneria Civile, Università di Firenze, Via Santa Marta 3, 50139 Firenze, Italy

(Received 25 February 1997 and in revised form 12 November 1997)

The axisymmetric boundary-layer separation of an incompressible impulsively started flow in a wavy-walled tube is analysed at moderate to high values of the Reynolds number. The investigation is carried out by numerical integration of either the Navier–Stokes equations or Prandtl’s asymptotic formulation of the boundary-layer problem. The presence of an adverse pressure gradient induces reverse flow at the tube wall independently of the Reynolds number; its occurrence can be predicted by a timescale analysis. Following that, the viscous calculations show different dynamics depending on the Reynolds number. As the Reynolds number increases, the boundary layer has in a well-defined internal structure where longitudinal lengthscales become comparable with the viscous one. Thus the boundary-layer scaling fails locally, with a minimum of pressure inside the boundary layer itself. The formation of the primary recirculation is well captured by the asymptotic model which, however, is not able to describe the roll-up of the vortex structure inside the recirculating region. This inadequacy appears well before the flow evolves to the characteristic terminal singularity usually assumed as foreshadowing the vortex shedding phenomenon. The outcomes are compared with the existing results of analogous problems giving an overall agreement but improving, in some cases, the physical picture.

1. Introduction

The separation of the boundary layer from a rigid surface is a common feature of a large variety of fluid dynamics problems. Classical examples are given by any stream flowing over an irregular boundary as well as by the motion of a body in a fluid otherwise at rest. Of particular relevance to this paper is the separation induced by external vortices which may result from previously separated vorticity or as a forerunner of wall turbulence structures.

Commonly, the separation of the boundary layer represents the rapid response to any modification in the external flow which induces a pressure growth along the direction of the motion. The adverse pressure gradient causes a deceleration in the wall flow which then has a tendency to detach. Because of its general relevance, the impulsively started case has been most commonly investigated. At low or moderate Reynolds number, the numerical solution of the Navier–Stokes equations is able to give a complete description of the flow. On the other hand, at large values of the Reynolds number, the Navier–Stokes formulation must be approximated by an asymptotic description in order to reduce the computational effort. Moreover, while the experimental studies at moderate Reynolds number are able to show the separation well, it is difficult to obtain a clear picture at high Reynolds number since the boundary layer is very thin and the phenomenon arises and develops at small spatial scales within the boundary layer.

A large number of flows with practical relevance are characterized by extremely high values of the Reynolds number, and these can be numerically solved only by using the asymptotic boundary layer approach originally formulated by Prandtl. The external pressure gradient which drives the phenomenon is often assumed to be caused by the wall geometry or by the presence of a rectilinear vortex convected above the surface; the latter represents the basis for effectively inviscid flows containing vorticity. The two-dimensional vortex-driven separation has been extensively studied by Doligalski & Walker (1984) for one vortex convected in a uniform flow and by Ersoy & Walker (1985, 1986) for counter-rotating vortex pairs near a wall, showing the creation of one vortex (respectively two vortices) within the boundary layer, of rotation opposite to the external inviscid vortex.

The results show the local thickening of the boundary layer terminating with the breakdown of the classical boundary-layer approximation in the form of a terminal singular behaviour of the solution. The failure of such an asymptotic scheme is generally interpreted as occurring when the thickness of the layer becomes comparable with the lengthscale of the external flow, and it is physically assumed to correspond to an ejection of vorticity.

The one-vortex case has also been investigated using the interacting boundary-layer technique (Chuang & Conlisk 1989), which takes into account the modification in the external flow field due to the boundary-layer thickening and consequently retards the appearance of the terminal singularity. This approach shows the splitting of the separated region with the formation of a secondary vortex within the boundary layer and a weak dependence of the flow evolution on the Reynolds number. A shear-layer region is also identified by the authors as a possible path to the ejection of the secondary vortex into the outer flow, which is still assumed to be the physical explanation of the mathematical singularity. The same problem has been solved using the Lagrangian technique (Peridier, Smith & Walker 1991 *a*) first introduced by Van Dommelen & Shen (1980), which is able to describe the flow up to the appearance of a singularity in the boundary-layer solution and in practice confirms the results obtained by Doligalski & Walker (1984). However, the authors found that the interacting theory coupled with the Lagrangian formulation (Peridier, Smith & Walker 1991 *b*) produces a singularity at a time earlier than that computed without interaction, contradicting the results obtained with the Eulerian formulation (Chuang & Conlisk 1989).

A numerical and experimental study of the boundary layer separation due to the impact of a vortex ring on a plane wall has been performed by Walker *et al.* (1987); the results obtained by solving the problem in the axisymmetric approximation show the typical behaviour of the separated region near the wall and a more abrupt boundary-layer growth than in the plane case. The authors pointed out that the classical theoretical approach is able to describe the formation of a separated vortex ring, but it is unable to capture the experimentally detected birth of a secondary vortex ring, which has the same direction of rotation of the first one. The classical Eulerian approach has been followed to study the dynamics of the boundary layer induced on a plane wall by a three-dimensional vortex loop (Ersoy & Walker 1987); the leading terms of the flow velocities are computed on and near the symmetry plane of the vortex. A variety of three-dimensional separation phenomena is detected, indicating the possibility of a developing eruption at spanwise locations away from the symmetry plane. Different separation patterns are detected depending upon whether the vortex moves towards the wall or recedes from it. An analogous analysis has been performed in the case of a rectilinear vortex filament approaching a spherical body by Pedrizzetti

(1992), which showed the influence of the initial distance between vortex and body surface upon the boundary-layer dynamics. The full three-dimensional boundary-layer problem has been numerically solved for a vortex approaching a cylinder (Affes, Xiao & Conlisk 1994), showing more complex separation patterns than the bidimensional problem; the reversed-flow region evolves to a three-dimensional separation ridge which is eventually ejected into the external stream.

The vortex-driven problem does not exhaust the variety of high-Reynolds-number flows investigated using the boundary-layer approximation, which also includes the impulsively started translating (Van Dommelen & Shen 1980; Henkes & Veldman 1987; Riley & Vasantha 1989) and roto-translating cylinder problem (Ece, Walker & Doligalski 1984). The translating cylinder problem has been studied using the Lagrangian approach (Van Dommelen & Shen 1980); the results are comparable with those obtained with the Eulerian approach (Henkes & Veldman 1987), both with classical and interactive formulation. In the latter work, the local splitting of the separated region into a double-layer structure has been observed by using the interacting model, which seems to give a better approximation of the Navier–Stokes solution at Reynolds number equal to 10^4 than the classical approach. Nevertheless, the authors point out that late in the calculation the boundary layer is probably too thick for the interaction model to be accurate. Riley & Vasantha (1989) investigated the same problem by solving the vorticity–streamfunction formulation in which no explicit assumption about the pressure gradient is required; by this method the calculation does not seem to become singular. These results are in agreement with those obtained at moderate Reynolds number by integrating the Navier–Stokes equations, up to the appearance of the first separated region. Afterwards, the solutions begin to diverge, suggesting different dynamics of the vorticity shedding as can be found in the pitching-up airfoil problems (Doligalski, Smith & Walker 1994 and references therein).

An analogous initial agreement between the Navier–Stokes and the boundary-layer solutions has been observed in the flow upstream of a cylinder–flat plate juncture. The unsteady separation has been studied at high Reynolds number (Puhak, Degani & Walker 1995) by coupling Eulerian and Lagrangian formulations of the classical boundary-layer approximation. The analysis of the flow in the plane of symmetry is related to experimental (Acarlar & Smith 1987; Smith, Fitzgerald & Greco 1991) and numerical results for moderate-Reynolds-number flows (Visbal 1991), demonstrating that the asymptotic description is able to capture the birth of the necklace vortex. At the final stage of calculation, in the boundary-layer solution there is sharp focusing of such a necklace vortex, while the numerical and experimental results for a wide range of Reynolds number show more complex dynamics (Baker 1979; Thomas 1987; Visbal 1991; Smith *et al.* 1991; Doligalski *et al.* 1994).

The results discussed above show a partial disagreement between the asymptotic analysis and the viscous observations in the boundary-layer evolution during a substantial period of time following the appearance of the primary circulation cell and preceding the shedding phenomenon. During this period of time, inside the boundary layer the major nonlinear development of vorticity takes place and thus a confirmed knowledge of the dynamics is relevant to many problems like, for example, the quantification of stresses or the prediction and control of the shedding phenomenon itself. However, in order to really distinguish the phenomena described at such small scales by a viscous simulation and to contrast them with the asymptotic prediction a careful comparison must be performed and definitive results are difficult to extract from data obtained by different authors for similar cases.

Another open question in the description of the boundary-layer dynamics by the

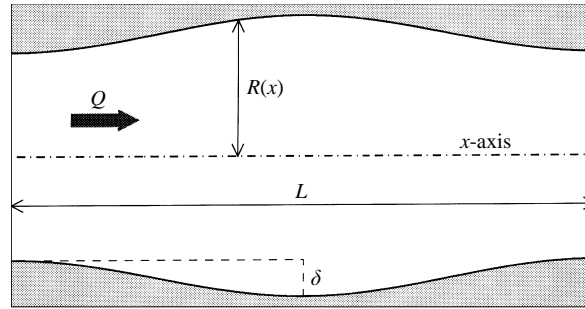


FIGURE 1. Sketch of the tube geometry.

Prandtl approximation is the physical significance of the terminal singular structure. This, which is also found in the interacting model, is generally seen as the mathematical failure of boundary-layer scaling when the scaled normal length tends to infinity because its physical value becomes of order of unity, corresponding to the shedding of vorticity. Furthermore it has been shown that the terminal structure is characterized by a mathematical singularity usually localized far from the wall (Van Dommelen & Cowley 1990) and several analyses of the nature of such a singularity have been performed in the Prandtl approach (Peridier *et al.* 1991 *a, b*; Cassel, Smith & Walker 1996). A parallel study of the boundary-layer evolution using a complete viscous calculation could be used to verify the physical interpretation of the terminal structure and possibly to find the location of the singularity in the regular viscous layer.

The present work concerns the impulsively started flow inside a wavy-walled duct. This represents a prototype for the class of problems in closed pipe systems characterized by strongly accelerating flows, which includes the transient dynamics of tube systems in engineering and biomedical fields, and a model problem for some cases of the systolic phase in circulatory systems. However the present work is focused on the idealized separation phenomenon and all additional complexities due to wall elasticity, fluid compressibility, or pre-existing flow inhomogeneities, including turbulence, are excluded.

The boundary-layer separation due to the enlargement of the section in a wavy-walled tube is studied here. The impulsively started condition is assumed by imposing an instantaneous value of the discharge. The Prandtl approach to the problem is numerically solved in the axisymmetric approximation by computing the inviscid bulk flow and the unsteady boundary-layer equations. In a circular geometry the assumption of axial symmetry is reasonable in the initial instants of a separating boundary layer; however, it will fail later once the vorticity has been shed into the bulk flow. The axisymmetric approximation allows a numerical resolution of the complete viscous problem governed by the Navier–Stokes equations which are integrated for several moderately high values of the Reynolds number. The dynamics of separation is analysed and a careful comparison between the viscous evolution and the asymptotic results is presented.

In what follows we will denote as *separation* the occurrence of a closed circulating cell, or a double vorticity layer, inside the boundary layer while, in order to avoid confusion, the phenomenon of ejection of vorticity outside the boundary layer will be referred as *shedding*.

2. Mathematical definition

2.1. The Navier–Stokes problem

Consider the axisymmetric motion of a viscous incompressible fluid, with kinematic viscosity ν and density ρ , in a wavy-walled tube due to a suddenly imposed flow rate Q_0^* . Let R_0 be the mean radius of the duct and U_0 the velocity averaged over the section of radius R_0 . Thus the discharge and tube radius are given by

$$Q_0^* = \pi R_0^2 U_0, \quad R^*(x^*) = R_0 R(x^*/R_0), \quad (1)$$

where x^* is the dimensional coordinate coincident with the tube axis. Choosing R_0 and U_0 as the unit length and velocity, respectively, the dimensionless discharge Q_0 is equal to π and the dimensionless radius of the tube is given by $R(x)$, which in the present work is assumed (figure 1) to be

$$R(x) = 1 - \frac{1}{2}\delta \cos(2\pi x/L). \quad (2)$$

Suppose that the pipe axis is the x -axis of a cylindrical system of coordinate $\{x, r, \theta\}$. Thus we can write the axisymmetric form of the Navier–Stokes equation in the vorticity–streamfunction formulation

$$\frac{\partial \omega}{\partial t} + \frac{1}{r} \frac{\partial \psi}{\partial r} \frac{\partial \omega}{\partial x} - \frac{1}{r} \frac{\partial \psi}{\partial x} \frac{\partial \omega}{\partial r} + \frac{\omega}{r^2} \frac{\partial \psi}{\partial x} = \frac{1}{Re} \left(\frac{\partial^2 \omega}{\partial x^2} + \frac{\partial^2 \omega}{\partial r^2} + \frac{1}{r} \frac{\partial \omega}{\partial r} - \frac{\omega}{r^2} \right), \quad (3)$$

where $\omega(x, r, t)$ is the azimuthal vorticity, $\psi(x, r, t)$ the Stokes streamfunction and $Re = R_0 U_0 / \nu$ the Reynolds number. The vorticity and streamfunction are related by the Poisson equation

$$-\omega r = \frac{\partial^2 \psi}{\partial x^2} + \frac{\partial^2 \psi}{\partial r^2} - \frac{1}{r} \frac{\partial \psi}{\partial r}, \quad (4)$$

the velocity field can be computed from the streamfunction (Batchelor 1967).

Equations (3) and (4) must be completed with boundary conditions. Periodicity is assumed in the x -direction. On the tube axis, the boundary conditions are given by symmetry considerations, resulting in

$$\omega = 0, \quad \psi = 0 \quad \text{at} \quad r = 0. \quad (5)$$

At the wall of the duct the velocity vector must vanish. A zero value for the normal velocity implies that the streamfunction is constant along the wall and proportional to the discharge flowing in the tube (Batchelor 1967). The condition of vanishing tangential velocity implies that the first-order normal derivative and the streamfunction and the second-order mixed derivative are zero. These, with equation (4), specify the value of the vorticity at the wall. The r -coordinate is changed by using a shearing transformation $r = zR(x)$ (Eiseman 1985; Ralph 1986); the z -coordinate is stretched by defining a ζ -coordinate as $z = \tanh(a\zeta)/\tanh(a)$, being a the stretching parameter (Pedrizzetti 1996). The complete formulation and details of the numerical procedure are described in Pedrizzetti (1996).

2.2. The boundary-layer problem

The case of impulsively started motion defined in the previous section can also be studied in the boundary-layer approximation. Consider a general system of coordinates $\{x_1^*, x_2^*, x_3^*\}$; in the present case, let x_1^* be the x -axis of the pipe, x_2^* be the θ -coordinate

of a cylindrical system and x_3^* the distance from the wall surface. Let $\{v_1^*, v_2^*, v_3^*\}$ be the velocity vector, where v_1^* and v_3^* are the tangential and normal components in the meridian plane, respectively, and v_2^* the θ -component. Define the following dimensionless variables:

$$\{x_1, x_2, x_3\} = \{x_1^*/R_0, x_2^*, Re^{1/2} x_3^*/R_0\}, \quad (6a)$$

$$\{v_1, v_2, v_3\} = \{v_1^*, v_2^*, Re^{1/2} v_3^*\}/U_0, \quad (6b)$$

$$t = \frac{t^* U_0}{R_0}, \quad p = \frac{p^*}{\rho U_0^2}. \quad (6c)$$

The boundary-layer equations of motion in the axisymmetric approximation are obtained by the Navier–Stokes equations written in a general orthogonal coordinate system neglecting higher-order terms with respect to $Re^{-1/2}$ (Crabtree, Küchemann & Sowerby 1963):

$$\frac{\partial v_1}{\partial t} + \frac{v_1}{h_1} \frac{\partial v_1}{\partial x_1} + v_3 \frac{\partial v_1}{\partial x_3} = -\frac{1}{h_1} \frac{\partial p}{\partial x_1} + \frac{\partial^2 v_1}{\partial x_3^2}, \quad (7)$$

$$\frac{1}{h_1 h_2} \frac{\partial(h_2 v_1)}{\partial x_1} + \frac{\partial v_3}{\partial x_3} = 0, \quad (8)$$

where $h_1 = (1 + R'(x)^2)^{1/2}$ and $h_2 = R(x)$. The no-slip condition at the wall, the matching with the external inviscid solution and the initial condition at $t = 0$, are respectively

$$v_1(x_1, x_3, t) = v_3(x_1, x_3, t) = 0 \quad \text{at} \quad x_3 = 0, \quad (9a)$$

$$v_1(x_1, x_3, t) \rightarrow U_1(x_1) \quad \text{as} \quad x_3 \rightarrow \infty, \quad (9b)$$

$$v_1(x_1, x_3, 0) = U_1(x_1); \quad (9c)$$

periodicity is assumed in the x_1 -direction, and U_1 is the inviscid flow velocity. The normal equation of motion in this asymptotic limit gives that pressure does not vary along x_3 , i.e. $p = p(x_1)$; thus the pressure gradient term in equation (7) can be written

$$\frac{U_1 \partial U_1}{h_1 \partial x_1} = -\frac{1}{h_1} \frac{\partial p}{\partial x_1}. \quad (10)$$

The inviscid velocity $U_1(x_1)$ is derived by numerically solving the zero-vorticity case of equation (4) and then computing the velocity component tangential to the wall.

In the numerical integration of (7) and (8), we introduced a stretched normal coordinate, $\eta = \log((x_3 + b)/b)$, ensuring a better resolution close to the wall, where b is the stretching parameter. The boundary layer equations (7) and (8) become

$$\frac{\partial v_1}{\partial t} + \frac{v_1}{h_1} \frac{\partial v_1}{\partial x_1} + v_3 \frac{\partial v_1}{\partial \eta} \frac{1}{be^\eta} = \frac{U_1 \partial U_1}{h_1 \partial x_1} + \frac{1}{(be^\eta)^2} \left(\frac{\partial^2}{\partial \eta^2} - \frac{\partial}{\partial \eta} \right) v_1, \quad (11)$$

$$\frac{1}{h_1 h_2} \frac{\partial(h_2 v_1)}{\partial x_1} + \frac{\partial v_3}{\partial \eta} \frac{1}{be^\eta} = 0, \quad (12)$$

which are numerically solved with the boundary condition (9a) imposed at $\eta = 0$ and condition (9b) imposed at a large, but finite, $\eta = \eta_{max}$. Equation (11) is integrated in

time by using an explicit fourth-order Runge–Kutta scheme; spatial derivatives are approximated with a centred second-order finite differences method. The velocity component v_3 is derived by integrating the continuity equation (12) on a staggered grid.

A number of different grid sizes and time steps have been used in order to define the appropriate computational resolution. First, the numerical results have been compared with the analytical solution of the rectilinear duct case, in order to check the influence of the stretching parameter b on the solution close to the wall surface. The same procedure has been performed in case of the wavy-walled tube (2), with $L = 5$, $\delta = 0.5$; a value for b around unity has been found to be appropriate. In this case the boundary layer has been seen to extend up to a distance of $x_3 \simeq 10$. Grid resolution has been tested by performing several runs, using $L = 5$, $\delta = 0.5$ and $b = 0.5$, with N_1 ranging between 64 and 1024 and N_3 from 24 to 96. No significant differences have been detected by varying the normal resolution. The axial resolution becomes important only late in the calculation, when a relevant velocity gradient appears in the x_1 -direction, but it does not influence the results in the major part of the flow evolution.

The time step has been selected in order to satisfy the diffusive and convective stability conditions. In the earliest stage of motion, when the boundary-layer thickness depends by viscous spreading only, the time step guarantees the proper resolution within the spacial grid if it is smaller than the smallest square grid length, Δx_{3min}^2 as ensured by the stability condition. However, a limitation on the early time accuracy is given by the non-zero normal grid spacing at the wall. In this case, using diffusive arguments, we can estimate that the solution is not accurate for $t < 4\Delta x_{3min}^2$; care has been used to keep such a value much smaller than physically relevant times; furthermore it has been checked for several cases that the subsequent evolution obtained with different time steps is not affected by this initial inaccuracy.

3. Impulsively started motion

3.1. The boundary layer solution

The time-dependent development of the boundary-layer solution is illustrated in figures 2 and 3. These plots show the instantaneous vorticity field and the streamline patterns, respectively, in the (x, η) -plane, for $L = 5$, $\delta = 0.5$. The calculations has been performed with a grid 1024×96 and a stretching parameter $b = 1$; the grid extends from the wall to $x_3 = 100$, resulting in $\Delta x_{3min} \simeq 0.05$; the time step is 1.2048. The vorticity is related to the velocity distribution by

$$\omega = \frac{\partial v_1}{\partial x_3} = \frac{\partial v_1}{\partial \eta} \frac{1}{be^\eta}; \quad (13)$$

the streamfunction is obtained by integration of the velocity field.

At $t = 0$, the motion is impulsively started from the rest and a thin viscous layer develops close to the rigid surface while diffusive terms let the vorticity spread normally to the wall. In the very initial stage of the motion, the boundary layer is almost symmetrical in the converging and diverging parts of the duct. The vorticity distribution at $t = 0.5$ is plotted in figure 2(a) and the corresponding instantaneous streamline pattern in figure 3(a). As time passes, the vorticity at the wall decreases and, at $t \simeq 0.7$, a separation point appears at $x \simeq 0.9$, forming a closed recirculating eddy attached to the wall. In figures 2(b) and 3(b) the flow pattern is illustrated at $t = 1$, a short time after the separation has occurred. Subsequently, the recirculation region close to the wall grows in the x -direction, showing the typical behaviour of the

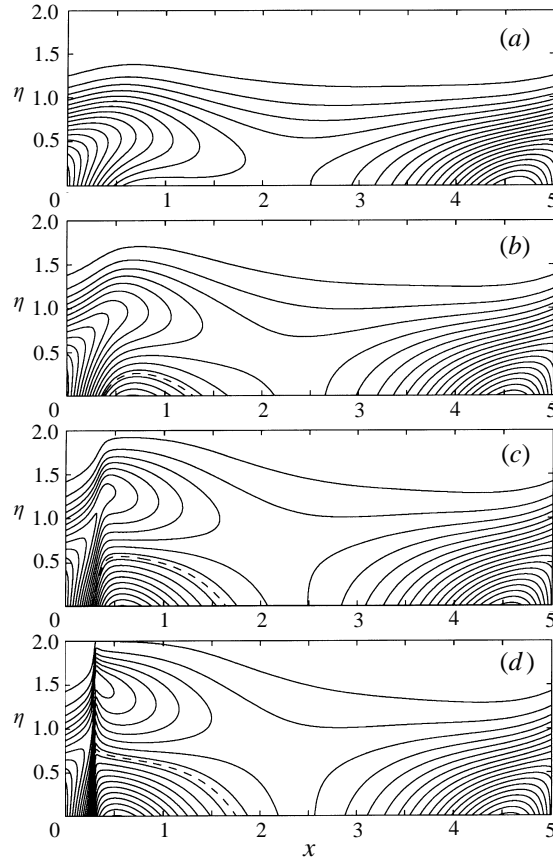


FIGURE 2. Instantaneous vorticity fields in the boundary layer for $\delta = 0.5$ at (a) $t = 0.5$, (b) $t = 1$, (c) $t = 1.5$, (d) $t = 1.75$. Contour levels from -1.05 to 1.95 , step 0.1 . Dashed line represents the zero level.

boundary-layer solution in the presence of an adverse pressure gradient (Doligalski & Walker 1984; Henkes & Veldman 1987). In such a model, the reverse motion on the wall side of the recirculating region is characterized by a favourable pressure gradient constant in time, which continuously pushes the flow back. After this, the localized rapid growth of the cell in a direction normal to the wall is observed at the upstream edge of the separated region, where the vorticity is concentrated (figures 2c and 3c), at $t = 1.5$. The final stage of the computed results is shown in figures 2(d) and 3(d), corresponding to $t = 1.75$; shortly after the numerical scheme fails to converge, at $t \simeq 1.85$. The vorticity distribution near the left-hand side of the eddy shows the typical spike-like behaviour, which is a forewarning of the terminal singularity of the solution. It is worth noting that the flow downstream the separated region, in the converging part of the duct, appears not to be influenced by the dynamics of the recirculation cell; that is, separation is essentially a local phenomenon. Furthermore, as can be seen from figure 2, the position of the singularity of the solution of boundary-layer problem is far from the wall surface as predicted by Van Dommelen & Cowley (1990). The flow development is qualitatively the same as found in previous boundary-layer calculations performed in different configurations, confirming that the initial stage of separation is completely driven by the external pressure gradient.

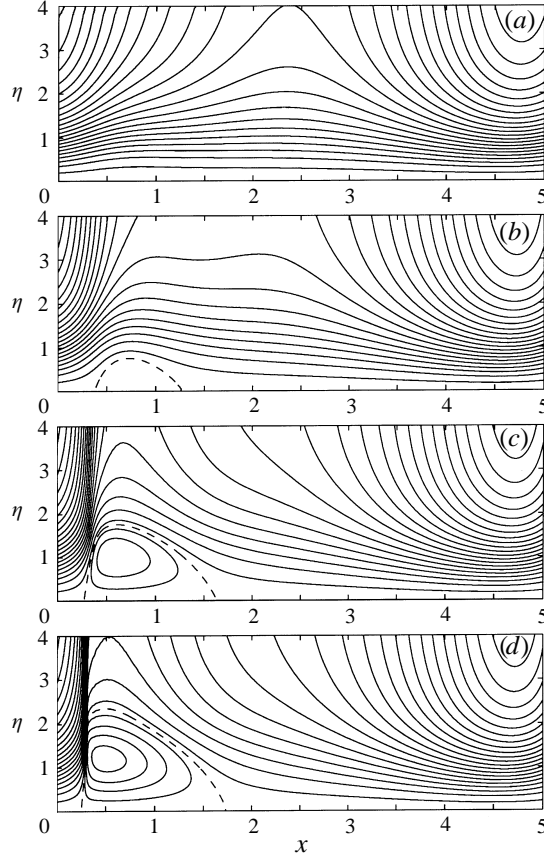


FIGURE 3. Instantaneous streamlines in the boundary layer for $\delta = 0.5$ at (a) $t = 0.5$, (b) $t = 1$, (c) $t = 1.5$, (d) $t = 1.75$. Streamfunction contour levels from -0.14 to 1 , step 0.04 . Dashed line represents the wall zero level.

The flow evolution described in figures 2 and 3 is dependent on the value of the perturbation parameter δ : small δ implies a weak pressure gradient, while large values of δ create a strong pressure gradient which accelerates the separation phenomenon. Nevertheless, the global behaviour of the flow field does not change qualitatively from the case $\delta = 0.5$ described above, and only the time of occurrence of the different phenomena varies with the external flow differences.

The dependence of the flow evolution on the value of δ can be predicted by a timescale analysis. Consider the inviscid bulk flow due to the dimensionless imposed discharge $Q_0 = \pi$ and let $U(x) = R(x)^{-2}$ be the average value of the longitudinal velocity over the section. A characteristic time of the problem can be defined as

$$T(\delta) = C \left\| \left(\frac{dU(x, \delta)}{dx} \right)^{-1} \right\|^n \frac{R_0}{U_0}, \quad (14)$$

with the standard definition for the n th-order norm in a domain \mathcal{D} given by

$$\|f\|^n = \left(\frac{1}{\mathcal{D}} \int_{\mathcal{D}} |f|^n d\mathcal{D} \right)^{1/n}, \quad (15)$$

where in (14) the domain is the interval $\mathcal{D} = [0, L]$.

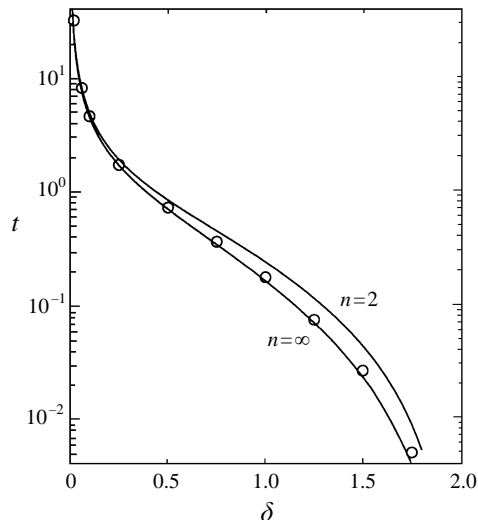


FIGURE 4. Separation time as a function of δ . Computed values from Prandtl simulations (\circ), analytical estimates (—).

The start of reversed flow corresponds to the appearance of zero wall vorticity at a certain time, say t_{sep} . In figure 4 the values of t_{sep} as derived by the numerical simulations with δ ranging between 0.02 and 1.75 are compared with $T(\delta)$ computed with $n = 2$ and $n = \infty$; the coefficient C is estimated as 0.57 and 0.44 for $n = 2$ and $n = \infty$, respectively, by performing a best-fitting procedure. A good agreement is observed between the results obtained numerically and the timescale analysis represented by equation (14). An analogous agreement, with different values of the coefficient C , is observed in the dependence on δ on the terminal time, here defined as the time of failure of the numerical scheme, but this is not reported here because of its non-rigorous definition.

Thus the modifications to the boundary-layer dynamics are contained in the external flow variations in a sort of self-similarity indicating that the boundary-layer solution up to separation does not hide any internal instability but is completely driven by the external inviscid velocity distribution. The simple argument outlined above is able to predict the occurrence of separation with varying external forcing.

3.2. The Navier–Stokes solution

The Navier–Stokes problem has been solved for $L = 5$ and $\delta = 0.5$, with Reynolds number ranging between 10^2 and 10^4 . The spatial resolution has been chosen by performing several runs with different numerical grids and different values of the stretching parameter a . No particular problems have been detected during this validation procedure. In what follows, the grid has been fixed to 128×48 , 256×64 and 512×64 and parameter a is 1.2, 1.5 and 3, for $Re = 10^2$, 10^3 and 10^4 , respectively. The time step has been chosen in order to satisfy the convective and diffusive stability conditions; its value is held constant at $1/2048$ in all cases; this value has been checked as accurately describing the flow after few initial time steps.

In figure 5 the instantaneous streamlines are plotted for $Re = 10^3$. At the initial stage of motion the flow is essentially irrotational and the vorticity is concentrated in a thin boundary layer close to the tube surface. In a purely diffusive problem the wall vorticity decreases uniformly along the wall; in the present case, the flow motion is retarded by

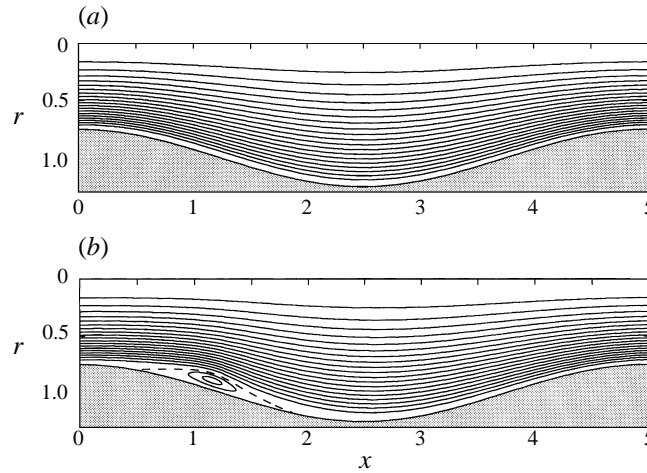


FIGURE 5. Instantaneous streamlines for $Re = 10^3$, $\delta = 0.5$ at (a) $t = 0.5$, (b) $t = 1.75$. Streamfunction contour levels from 0 to 0.5, step 0.025, and from 0.5 to 0.55, step 0.01. Dashed line represents the wall level.

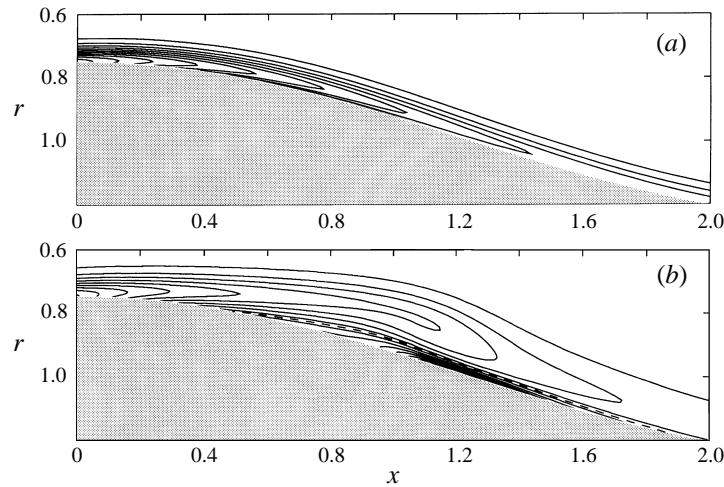


FIGURE 6. Instantaneous vorticity fields for $Re = 10^3$, $\delta = 0.5$ at (a) $t = 0.5$, (b) $t = 1.75$. Contour levels from -37.5 to 62.5 , step 5. Dashed line represents the zero level.

the adverse pressure gradient due to the enlargement of the wall profile. Then a decrease of the wall vorticity and the consequent appearance of a separation point, as outlined in the previously reported boundary-layer approximation, are expected. The streamlines at $t = 0.5$ are reported in figure 5(a). The flow is almost irrotational, as can be seen by the symmetry of the streamline pattern. At $t \simeq 0.7$ a separation point appears at the wall, at $x \simeq 0.9$. A more marked interaction starts to develop between the boundary-layer flow and the irrotational bulk flow, which is gradually displaced. As the reverse flow appears, the separation point rapidly moves backward and the attachment point downstream. The flow field at $t = 1.75$ is reported in figure 5(b), where the separated region can be observed. At this time, we can recognize a well-defined vortex in the central region of the recirculation cell.

An enlarged view of the flow evolution described above is reported in figure 6, where the instantaneous vorticity fields are plotted. At $t = 0.5$, figure 6(a), a minimum in the

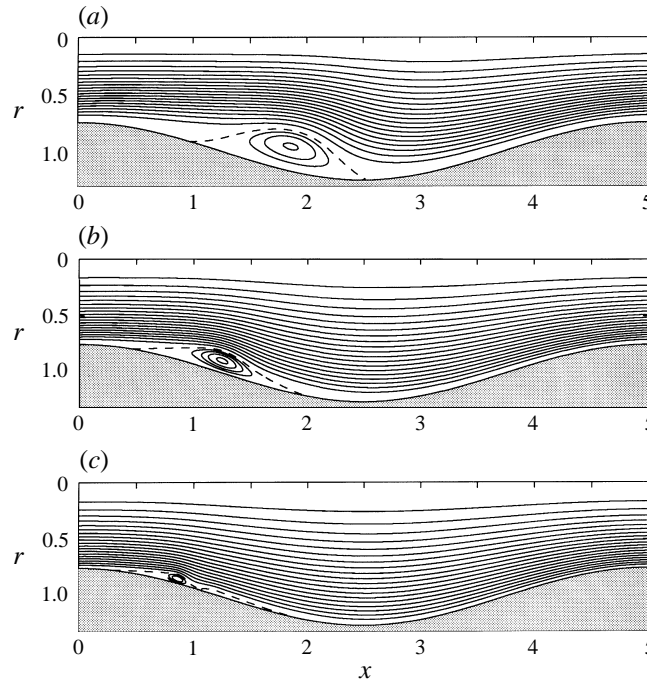


FIGURE 7. Instantaneous streamlines at $t = 2$ for $\delta = 0.5$: (a) $Re = 10^2$, (b) $Re = 10^3$, (c) $Re = 10^4$. Streamfunction contour levels from 0 to 0.5, step 0.025, and from 0.5 to 0.55, step 0.01. Dashed line represents wall level.

vorticity distribution at the wall is observable, due to the decelerating flow. The presence of the separated region locally increases the boundary-layer thickness; the value of the wall vorticity decreases further on, as a consequence of the backward acceleration of the flow. Then, the vorticity begins to concentrate in the central part of the reversed-flow region, causing the formation of a central vortex structure, figure 6(b) corresponding to $t = 1.75$. At this time of calculation, the vorticity is still concentrated in the boundary layer at the wall while the bulk flow is irrotational, and the injection of wall vorticity in the main flow has not been detected.

The initial dynamics of the flow field does not show significant differences on varying Reynolds number in the range 10^2 – 10^4 , with the exception of the boundary-layer thickening, which is primarily due to the vorticity diffusion; thus the typical boundary-layer lengthscale in a direction normal to the wall is proportional to $Re^{-1/2} t^{1/2}$. At $t \simeq 0.7$ a separation point is observed to appear at the wall, for every Re analysed in the present work; the position of the point moves slightly backward as Re increases. Then the recirculating region elongates tangentially to the wall. Once the separated region has formed the flow evolution becomes more dependent on the Reynolds number. At low values of Re , say $Re \simeq 10^2$ corresponding to substantially viscous flow, the recirculating region grows until it completely fills the enlargement of the tube before any actual ejection of vorticity occurs. The flow at larger Reynolds number, characterized by a weaker diffusive contribution, has higher values of vorticity in a thinner layer at the wall and a vorticity gradient which becomes stronger as Reynolds number increases. As we have outlined for $Re = 10^3$, figures 5 and 6, the vorticity concentrates into a vortex in the middle of the separated region and the locally reversed limiting velocity is able to cause a secondary separation.

In figure 7 the instantaneous streamlines at various Reynolds number are reported, corresponding to $t = 2$. At this time, the separated region shows the central vortex structure for Re equal to 10^3 and 10^4 . The vortex appears to be strong enough to induce a secondary separation, as can be seen in figure 7(c) for $Re = 10^4$. Afterwards, the vorticity inside of the secondary eddy is compressed in a direction tangential to the wall and then ejected into the irrotational bulk stream. The interaction between the erupted plume and the mainstream causes the cut-off and shedding of the primary vortex. The phenomenon occurs at $t = 1.79$ for $Re = 10^4$; the same sequence has been found for $Re = 10^3$, with the secondary separation occurring at $t = 2.09$. The calculation for $Re = 10^2$ has been carried out until $t = 10$ but neither the secondary separation nor the shedding of vorticity have been detected.

4. Comparison between Navier–Stokes and Prandtl solutions

The comparison of the results obtained by solving the Navier–Stokes equations and the boundary-layer formulation of the problem is a primary objective of this work. The instantaneous vorticity fields resulting from the two different approaches are plotted in figure 8; in order to achieve a qualitative comparison between the results, the coordinate x_3 and the vorticity value of the boundary-layer solution are respectively divided and multiplied by $Re^{-1/2}$, where $Re = 10^4$ is the corresponding Reynolds number of the Navier–Stokes solution. The vorticity fields at $t = 0.5$ are reported in figure 8(a) and 8(b), for the Navier–Stokes and Prandtl approach, respectively. The comparison shows excellent agreement between the solutions. It is important to notice that at this stage of motion the flow is completely attached to the wall. In figures 8(c) and 8(d) the fields are plotted at $t = 1.75$, showing different dynamics of the reversed flow region. The boundary-layer approach gives the typical vorticity distribution inside the separated region, see also figure 2(d); the interaction between the upstream flow and the reversed flow within the separated region induces the localization of a strong vorticity gradient in the upward part of the recirculating region. On the other hand, the Navier–Stokes solution is characterized by the localization of this gradient in the middle of the separated region, corresponding to a well-defined vortex structure inside the boundary layer as it has been described in §3.2.

The space–time evolution of the wall vorticity can give a global perspective to analyse the dynamics of the flow as a whole; results obtained at different values of the Reynolds number and from the asymptotic computation are reported in figure 9. In the initial stage of motion, the boundary-layer evolution is completely driven by the irrotational bulk flow. The vorticity distribution at the wall is not qualitatively influenced by the Reynolds number, whose effect consists in scaling the boundary-layer thickness, that is the lengthscale in a direction normal to the wall, and consequently the value of the wall shear stress. Before the separation has appeared, the results obtained show a good agreement between the Prandtl and Navier–Stokes approaches, as pointed out by Henkes & Veldman (1987) and Riley & Vasantha (1989) for the impulsively started cylinder problem. The separation occurs at $t \simeq 0.7$, both in the boundary-layer solution and in the Navier–Stokes ones for all the Reynolds number investigated here. The position of the separation point appears to be weakly dependent on the Reynolds number, and moves backward as Re increases, showing the expected convergence of the Navier–Stokes results to those obtained by the Prandtl formulation. Once the separation has occurred, a region of negative counterclockwise vorticity develops at the wall. At low Reynolds number, see figure 9(a) at $Re = 10^2$, the recirculating cell dynamics is dominated by the diffusive effects. The vorticity layer at

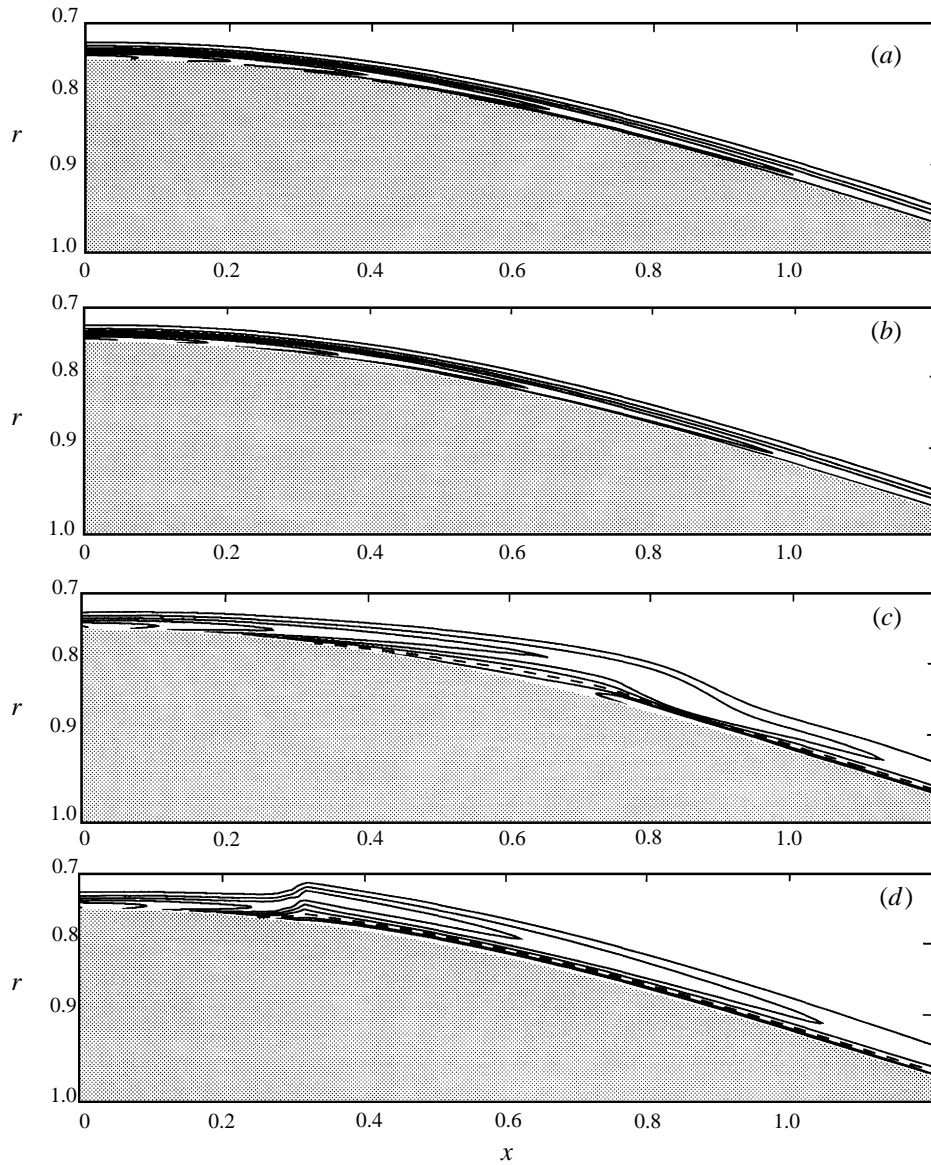


FIGURE 8. Instantaneous vorticity fields at $t = 0.5$: (a) Navier–Stokes solution $Re = 10^4$; (b) Prandtl solution; $t = 1.75$; (c) Navier–Stokes solution $Re = 10^4$; (d) Prandtl solution. Contour levels from 10 to 150 (a, b) and -40 to 120 (c, d), step 20. Dashed line represents the zero level. Prandtl solution is scaled to allow proper comparison.

the wall rapidly fills the hollow of the tube. The irrotational flow is confined in the central part of the duct, resulting in an almost rectilinear stream and the boundary layer becomes indistinguishable. The adverse pressure gradient gradually weakens and the flow field evolves to a steady configuration. When the Reynolds number is higher the evolution after the first separation differs significantly; this can be observed by comparing figures 9(b) and 9(c) at $Re = 10^3$ and $Re = 10^4$, respectively. Shortly after the first separation, the vorticity distribution at the wall shows a smooth minimum inside the separated region. As the flow evolves the negative vorticity upstream of the

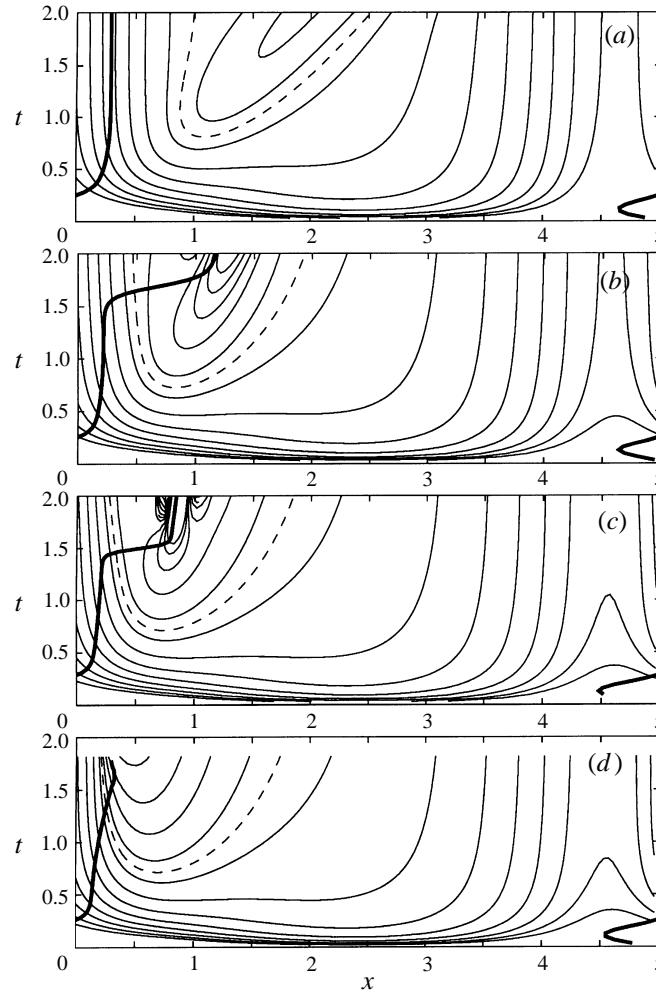
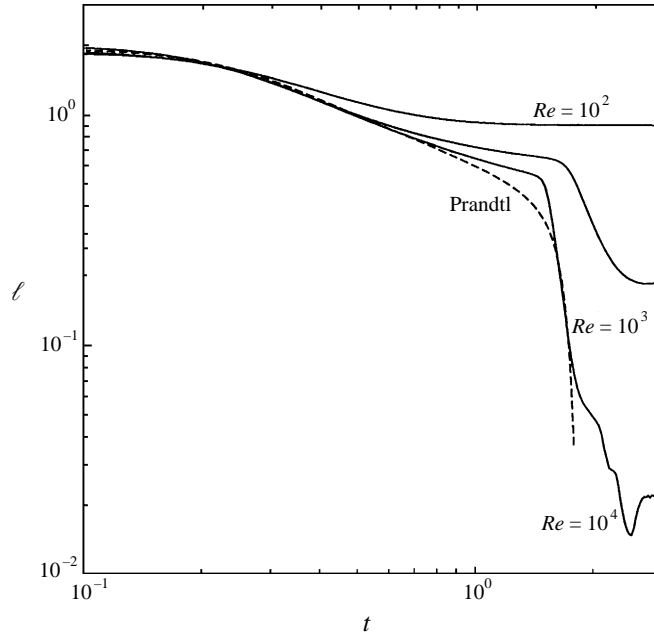


FIGURE 9. Wall vorticity space–time evolution; (a) $Re = 10^2$, (b) $Re = 10^3$, (c) $Re = 10^4$, (d) Prandtl solution. Thick lines represent the path of the barycentre X_b .

minimum begins to grow while the minimum decreases rapidly, this is reflected in a local growth of the boundary-layer thickness. This process, see $t \simeq 1.5$, leads to a strong vorticity gradient tangent to the surface localized in the central zone of the recirculating cell, as is observable in figures 9(b) and 9(c). Thus the inner flow develops variations on a short longitudinal lengthscale which is no longer comparable with an external flow scaling but, rather, with a viscous length. At $t \simeq 1.8$, a region of positive clockwise vorticity appears for $Re = 10^4$, corresponding to a secondary separation, figure 9(c); for $Re = 10^3$, this phenomenon occurs at $t > 2$, and it is only foreshadowed at this time of calculation, figure 9(b). In the Prandtl approach, figure 9(d), the boundary-layer dynamics is continuously forced by the inviscid adverse pressure gradient, which is not influenced by the boundary-layer evolution. Thus, the reversed flow is accelerated upstream and the vorticity gradient concentrates in the upper limit of the recirculating region.

The wall vorticity evolution is suggestive of the behaviour of the whole boundary-layer vorticity field. A global measure of the boundary-layer behaviour can be perceived by looking at the time evolution of a typical minimum tangential lengthscale

FIGURE 10. Time evolution of the longitudinal lengthscale ℓ .

and its localization in the flow field. In order to not be subjected to the numerically ambiguous evaluation of extreme values, a typical longitudinal lengthscale is evaluated as

$$\ell(t) = \left[\int \omega^n dA \right]^{1/n} / \left[\int \left(\frac{\partial \omega}{\partial \tau} \right)^n dA \right]^{1/n}, \quad (16)$$

where the integral is computed over the whole flow field and τ is the tangential direction. The lengthscale defined in (16) can be regarded, when n is large enough, as the inverse of the maximum vorticity gradient, normalized with the vorticity. The localization in space of the most relevant longitudinal variations is evaluated from

$$X_\ell(t) = \frac{L}{2\pi} \tan^{-1} \left(\frac{\int \left(\frac{\partial \omega}{\partial \tau} \right)^n \sin(2\pi x/L) dA}{\int \left(\frac{\partial \omega}{\partial \tau} \right)^n \cos(2\pi x/L) dA} \right) \quad (17)$$

which corresponds to the barycentre of the n th moment of the distribution of the tangent vorticity gradient computed over the whole flow field, assuming periodicity in the x -direction. In figure 9 the space–time evolution of the quantity defined in (17) is plotted for $n = 8$. No qualitative difference has been observed on varying n in the evaluation of (16) and (17). The barycentre path shows a slow variation for $Re = 10^2$, figure 9(a). Its position shows an abrupt deviation at $t \simeq 1.4$ and $t \simeq 1.6$ for $Re = 10^4$ and 10^3 respectively, moving from the upstream edge of the primary separated region to the edge of the secondary one, figures 9(b) and 9(c). On the other hand, the Prandtl results show that during the flow evolution such a position always corresponds to the upstream edge of the recirculation region, figure 9(d). Furthermore, in the Navier–Stokes solution the maximum occurs at the wall, while in the Prandtl solution the terminal singularity is expected to appear far from the surface (Van Dommelen & Cowley 1990).

In figure 10 the time evolution of the longitudinal length scale ℓ is reported for

$n = 8$, showing a good convergence between the Prandtl solution and the Navier–Stokes solutions, computed at various Reynolds number, up to $t \simeq 0.3$. This period corresponds to the initial development of the boundary-layer flow due to the inviscid pressure gradient distribution, and ℓ is essentially an external length scale of $O(1)$. As time increases the value of ℓ slowly decreases, with slight differences among the asymptotic and the viscous cases, until shortly after the first separation. These differences are more marked at low Reynolds number and are imputable to the diffusive effects. Afterwards, the Prandtl solution shows a continuous regular decreasing of ℓ , as can be expected from the flow evolution reported in figure 2: the flow dynamics presents an increasing vorticity gradient at the edge of the separation cell, until the defined lengthscale becomes comparable with the grid resolution and the computation fails to converge. The failure depends on a characteristic of the unsteady boundary layer equations, which has been theoretically demonstrated to approach a singularity at a finite time (Van Dommelen & Cowley 1990); the numerical scheme only anticipates this phenomenon. On the other hand, the Navier–Stokes solution confirms the dependence on the Reynolds number. At $Re = 10^4$, ℓ is $O(1)$ till $t \simeq 1.4$, and then it dramatically decreases; this occurs at the same instant as the deviation of the barycentre path, reported in figure 9(c), and it is predictive of the secondary separation. Such a behaviour can also be observed for $Re = 10^3$, at $t \simeq 1.6$.

5. Discussion

The results obtained by solving the Navier–Stokes equations are in excellent agreement with the classical boundary-layer approximation until the appearance of the primary separation and the birth of a region of reversed flow close to the wall surface. Before the first separation, the boundary-layer flow is driven by the irrotational bulk flow, which gives the timescale of the phenomenon; the first separation appears at $t \simeq 0.7$ both for the Navier–Stokes and Prandtl solutions, and the small differences we have found can be attributed to a weak influence of the viscous effects. As time proceeds, the separated region dynamics becomes more influenced by the internal boundary layer scaling which depends quantitatively on viscosity well before shedding. At low Reynolds number, the secondary separation has not been detected. As the Reynolds number increases, the viscous solution grows in complexity. The recirculating cell evolves to a secondary separation, which is the typical condition at the ejection of the wall vorticity in the external irrotational flow (Doligalski *et al.* 1994, and references therein). The secondary separation appears as an internal phenomenon of the boundary layer where the role of the external solution is placed locally by the vortex contained inside the boundary layer. The time of appearance of the secondary separation does not show a significant variation for $Re = 10^3$ and 10^4 , being 2.09 and 1.79 respectively, suggesting, because of the lower bound given by the primary separation, a slightly smaller asymptotic value for higher Reynolds number. In these two cases, the primary and secondary separations develop within the boundary layer and the shedding of vorticity is a subsequent phenomenon.

The presence of a secondary separation is not the only difference between the Navier–Stokes and Prandtl results. We have shown in the preceding section that secondary separation is anticipated by other facts. After the first separation, the vorticity steepens at the upstream edge of the separated cell where the smallest longitudinal lengthscale is localized. Then, in viscous flow only, a strong vorticity gradient appears in the middle of the cell foreshadowing the second separation. At this time the minimal longitudinal lengthscale in the flow moves to the central part of the

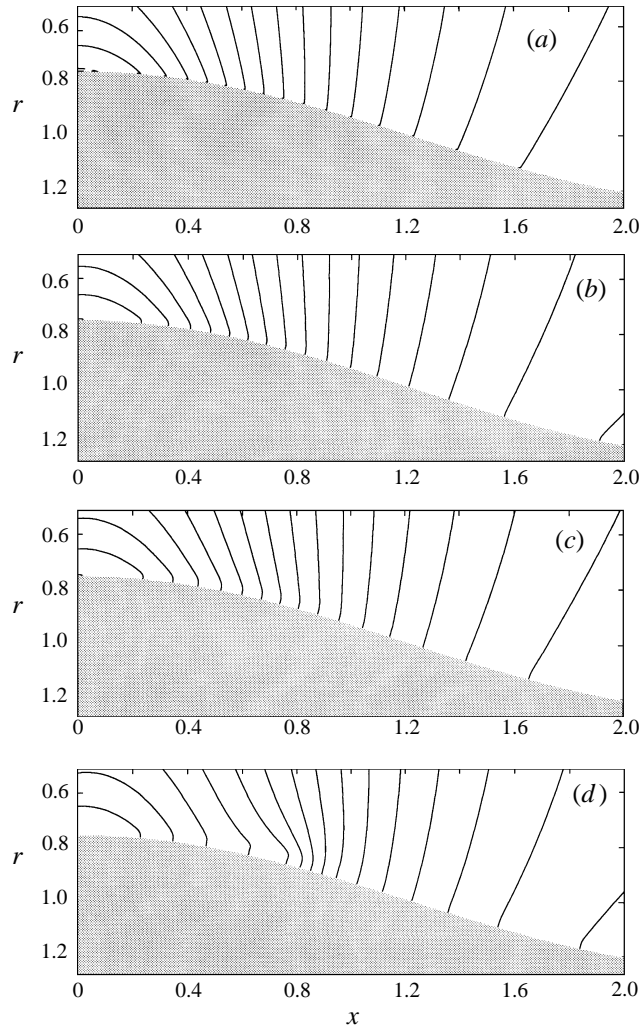


FIGURE 11. Instantaneous pressure fields: (a) irrotational, $Re = 10^4$; (b) $t = 0.5$, (c) $t = 1$, (d) $t = 1.5$. Isobars levels are separated by 0.1 units.

cell and its value abruptly decreases, to viscous values. At this point a failure of the Prandtl scaling can be related to the local presence of a longitudinal length comparable with the normal one. Such a process, which precedes the secondary separation and occurs earlier as the Reynolds number increases, is completely absent in the boundary-layer approximation, and it is evident well before the occurrence of the terminal structure of the Prandtl solution.

This different behaviour has been also detected by comparing the solutions obtained by solving the Navier–Stokes equations and the boundary-layer approximation for many problems, e.g. the impulsively started cylinder (Henkes & Veldman 1987; Riley & Vasantha 1989), the motion upstream of an obstacle (Puhak *et al.* 1995; Visbal 1991), the impact of a vortex ring on a wall (Walker *et al.* 1987; Orlandi & Verzicco 1993).

The Prandtl solution is not able to describe the secondary separation and evolves to a singularity. However, the singular behaviour does not represent the inability to reproduce a secondary separation. This is also confirmed by the results obtained with

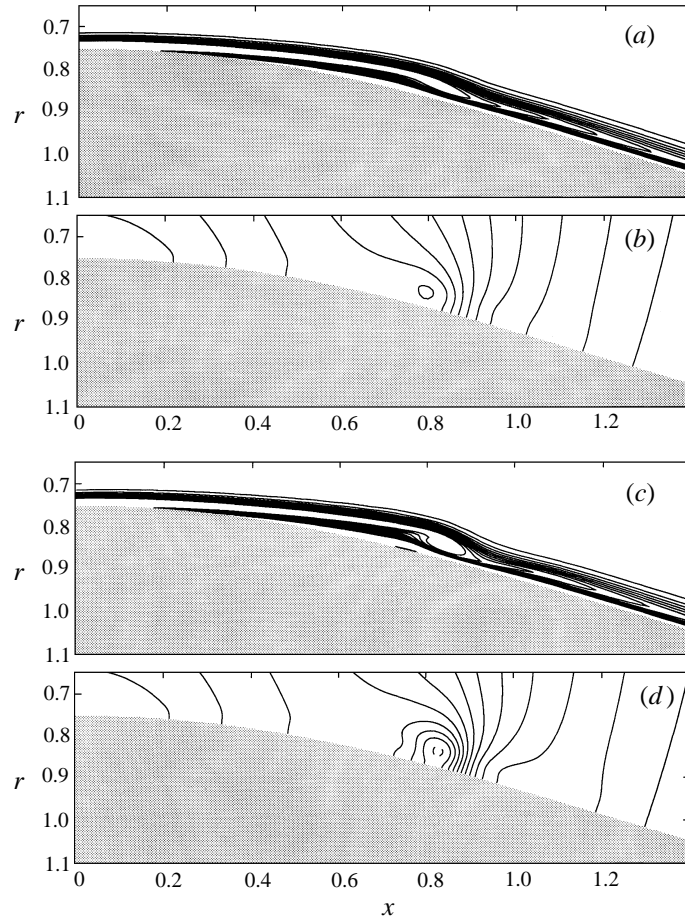


FIGURE 12. Instantaneous vorticity and pressure fields for $Re = 10^4$: (a) vorticity, (b) pressure at $t = 1.65$; (c) vorticity, (d) pressure $t = 1.85$. Isobars levels are separated by 0.1 units. Vorticity contour levels from 2.5 to 52.5, step 5.

the interacting boundary-layer approach, which show the same singular behaviour of the classical Prandtl solution, but just before the failure of the numerical scheme is able to describe the splitting of the first recirculating cell and the birth of a small secondary separation (Henkes & Veldman 1987; Riley & Vasantha 1989; Peridier *et al.* 1991*b*). The local inversion of the pressure gradient is enough to split the primary recirculating cell and generate a secondary separation. This approach considers the effect of the interaction only in the boundary condition of the problem, while the structure of the equations of motion is retained; in particular the pressure field, which is kept frozen in the Prandtl approach, is allowed to change longitudinally in time while a constant pressure distribution orthogonally to the wall is still assumed.

In order to clarify the influence of the variation in the pressure distribution on the separated boundary layer, the pressure field has been computed by integration from the solution of the Navier–Stokes equations. The irrotational pressure field is reported in figure 11(a) and we remind readers that this is the pressure field corresponding to every instant of the Prandtl solution. In figure 11(b) the pressure distribution at $t = 0.5$ is plotted for $Re = 10^4$, showing very small differences with the initial irrotational one, which result from the small unavoidable influence of viscous resistance. After the first

separation has occurred, see figure 11(c) at $t = 1$, a small distortion in the pressure field due to the growing recirculating cell is observable; this is more evident in figure 11(d) corresponding to $t = 1.5$. At this time the pressure along the wall is different from the original field reported in figure 11(a), and it is substantially constant normally to the surface inside the boundary layer whose thickness can even be defined by this pressure property. These small longitudinal variations in pressure, neglected in the Prandtl model, can be reproduced in the interacting boundary-layer approach. It must be kept in mind that at this point the boundary-layer vorticity field has not rolled up into a recognizable vortex and, with this value of Re , this corresponds about to the time where the transition from one type of Prandtl behaviour to a different one, which precedes the secondary separation, is occurring (see figures 9 and 10).

At subsequent times the boundary-layer vorticity contained inside the circulating cell begins to roll up into a well-defined vorticity structure. This phenomenon occurs at viscous scales but its dynamics is driven by an inviscid vortex sheet instability and occurs very rapidly. The local vorticity field at $t = 1.65$ is reported in figure 12(a) where a vorticity structure, undoubtedly contained inside the boundary layer, begins to show up. The development of such a vortex structure is accompanied by the presence of a pressure structure whose corresponding field is reported in figure 12(b); this is characterized by the typical minimum of pressure inside the vortex. This phenomenon is far more evident at $t = 1.81$ reported in figure 12(c, d). At this time there is still no evidence of any shedding and rather a structured boundary layer containing a well-defined vortex is found. The pressure field varies locally both in the tangential and in the normal directions.

Commonly, the terminal structure of the boundary-layer solution is considered the foreshadowing of the injection of the wall vorticity in the otherwise irrotational external flow. In mathematical terms the singularity represents the failure of the boundary-layer scaling due to growth of the normal lengthscale up to the outer flow; in physical terms this corresponds to the phenomenon of shedding. In the present case this picture does not apply. The failure of the asymptotic scaling occurs, in physical terms, well before shedding and, in the Prandtl solution, well before the terminal singular behaviour. It is determined by a local decrease of the longitudinal length up to the viscous scale. This abrupt reduction is not related to an eruption of the boundary layer and occurs corresponding to a roll-up of the primary vorticity layer in the middle of the circulating cell; the minimum longitudinal length localizes at the wall and has no relation to the singularity found far from the wall in the asymptotic formulation. The formation of a vorticity structure inside of the boundary layer is accompanied by a strong local pressure variation. This is the proof of the failure of Prandtl scaling which would imply that the normal equation of motion simplifies to constant pressure along this direction.

6. Conclusions

The impulsively started flow in a wavy-walled tube due to a constant imposed discharge has been investigated. It represents a prototype model for the separation dynamics in non-uniform closed pipe systems during transient flow characterized by a rapid acceleration. The problem has been studied by numerically solving both the Navier–Stokes equations at various Reynolds number and the Prandtl asymptotic formulation.

The general separation dynamics has been analysed. In the early stage of motion the flow is essentially irrotational, with the exception of a thin layer of vorticity close to the tube surface. The flow evolution is weakly influenced by the Reynolds number until the

first separation has occurred. The pressure distribution of the inviscid bulk flow drives the phenomenon, whose timescale can then be computed explicitly *a priori*. This has been verified by integration of the boundary-layer problem with varying wall profile steepness.

Once the primary separation has occurred, the differences between the two approaches increases as time passes. The Prandtl solution evolves to a terminal singularity, characterized by the concentration of vorticity in the upstream edge of the recirculating cell. On the other hand, the Navier–Stokes solution begins to depend on the Reynolds number. As the Reynolds number increases, the primary separated vorticity departs from the asymptotic model dynamics. The strongest vorticity gradient along the wall moves from the edge of the cell to the middle part of the recirculating region and organizes itself in an easily recognizable vortex structure contained inside the boundary layer. This is characterized by a local reduction of the longitudinal lengthscale to values comparable with the boundary-layer thickness. The vortex development is associated with the appearance, within the boundary layer, of a local minimum in the pressure distribution, which cannot be captured in the Prandtl formulation of the problem. Even though the boundary layer is still of small thickness, consistent with the Prandtl scaling, such a scaling fails locally inside the boundary layer and the evolution leading to the terminal singular structure does not have a physical counterpart in the high-Reynolds-number problem.

The common interpretation for the failure of the asymptotic scaling as due to the local growth of the boundary-layer thickness and, physically, to shedding of vorticity into the outer flow does not apply to the present case. The failure is here shown to be associated with the presence of a vorticity structure of comparable longitudinal and normal dimensions contained inside the boundary layer itself.

The validity of these observations cannot be directly extended to different boundary-layer flows. In fact this is an internal axisymmetric problem, thus pressure variations reflect strongly in the field constrained in a closed geometry and the motion of vorticity from the wall implies a compression of circular vortex lines with the consequent variation of enstrophy. These two constraints are not present in a two-dimensional boundary-layer flow. Particular care must be taken in transferring the results to the case of vortex-induced separation. In the present work the inviscid external flow represents transport in a direction tangent to the wall which is not favourable to an eruption of vorticity. The limiting external velocity in vortex-induced boundary-layer problem usually contains stagnation points and a compression towards the separating saddle; thus a thickened boundary layer has a tendency to erupt, driven by the external velocity boundary condition, and the viscous–inviscid interaction drives the flow normally from the surface rather than tangentially.

REFERENCES

- ACARLAR, M. S. & SMITH, C. R. 1987 A study of hairpin vortices in a laminar boundary layer. Part I. Hairpin vortices generated by a hemisphere protuberance. *J. Fluid Mech.* **175**, 1–41.
- AFFES, H., XIAO, Z. & CONLISK, A. T. 1994 The boundary-layer flow due to a vortex approaching a cylinder. *J. Fluid Mech.* **275**, 33–57.
- BAKER, C. J. 1979 The laminar horseshoe vortex. *J. Fluid Mech.* **95**, 347–367.
- BATCHELOR, G. K. 1967 *An Introduction to Fluid Dynamics*. Cambridge University Press.
- CASSEL, K. W., SMITH, F. T. & WALKER, J. D. A. 1996 The onset of instability in unsteady boundary-layer separation. *J. Fluid Mech.* **315**, 223–256.
- CHUANG, F. S. & CONLISK, A. T. 1989 The effect of interaction on the boundary layer induced by a convected rectilinear vortex. *J. Fluid Mech.* **200**, 337–365.

- CRABTREE, L. F., KÜCHEMANN, D. & SOWERBY L. 1963 Three-dimensional boundary layer. In *Laminar Boundary Layers*, 1st edn (ed. L. Rosenhead). Oxford University Press.
- DOLIGALSKI, T. L., SMITH, C. R. & WALKER, J. D. A. 1994 Vortex interactions with wall. *Ann. Rev. Fluid Mech.* **26**, 573–616.
- DOLIGALSKI, T. L. & WALKER, J. D. A. 1984 The boundary layer induced by a convected rectilinear vortex. *J. Fluid Mech.* **139**, 1–30.
- ECE, M. C., WALKER, J. D. A. & DOLIGALSKI, T. L.. 1984 The boundary layer on an impulsively started rotating and translating cylinder. *Phys. Fluids A* **27**, 1077–1089.
- EISEMAN, P. R. 1985 Grid generation for fluid mechanics computation. *Ann. Rev. Fluid Mech.* **17**, 487–522.
- ERSOY, S. & WALKER, J. D. A. 1985 Viscous flow induced by counter-rotating vortices. *Phys. Fluids A* **28**, 2687–2698.
- ERSOY, S. & WALKER, J. D. A. 1986 Flow induced at a wall by a vortex pair. *AIAA J.* **24**, 1597–1605.
- ERSOY, S. & WALKER, J. D. A. 1987 The boundary layer due to a three-dimensional vortex loop. *J. Fluid Mech.* **185**, 569–598.
- HENKES, R. A. W. M. & VELDMAN, A. E. P. 1987 On the breakdown of the steady and unsteady interacting boundary-layer description. *J. Fluid Mech.* **179**, 513–529.
- ORLANDI, P., VERZICCO, R. 1993 Vortex rings impinging on walls – axisymmetric and 3-dimensional simulations. *J. Fluid Mech.* **256**, 615–646.
- PEDRIZZETTI, G. 1992 Close interaction between a vortex filament and a rigid sphere. *J. Fluid Mech.* **245**, 701–722.
- PEDRIZZETTI, G. 1996 Unsteady tube flow over an expansion. *J. Fluid Mech.* **310**, 89–111.
- PERIDIER, V. J., SMITH, F. T. & WALKER, J. D. A. 1991a Vortex-induced boundary-layer separation. Part 1. The unsteady limit problem $Re \rightarrow \infty$. *J. Fluid Mech.* **232**, 99–131.
- PERIDIER, V. J., SMITH, F. T. & WALKER, J. D. A. 1991b Vortex-induced boundary-layer separation. Part 2. Unsteady interacting boundary-layer theory. *J. Fluid Mech.* **232**, 132–165.
- PUHAK, R. I., DEGANI, A. T. & WALKER, J. D. A. 1995 Unsteady separation and heat transfer upstream of obstacles. *J. Fluid Mech.* **305**, 1–27.
- RALPH, M. E. 1986 Oscillatory flow in wavy-walled tubes. *J. Fluid Mech.* **168**, 515–540.
- RILEY, N. & VASANTHA, R. 1989 Unsteady high-Reynolds-number flows. *J. Fluid Mech.* **205**, 243–262.
- SMITH, C. R., FITZGERALD, J. P. & GRECO, J. J. 1991 Cylinder end-wall vortex dynamics. *Phys. Fluids A* **3**, 2031.
- THOMAS, A. S. W. 1987 The unsteady characteristic of laminar juncture flow. *Phys. Fluids A* **30**, 283–285.
- VAN DOMMELEN, L. L. & COWLEY, S. J. 1990 On the Lagrangian description of unsteady boundary-layer separation. Part 1. General theory. *J. Fluid Mech.* **210**, 593–626.
- VAN DOMMELEN, L. L. & SHEN, S. F. 1980 The spontaneous generation of the singularity in a separating boundary layer. *J. Comput. Phys.* **38**, 125–140.
- VISBAL, M. R. 1991 Structure of laminar juncture flows. *AIAA J.* **29**, 1273–1282.
- WALKER, J. D. A., SMITH, C. R., CERRA, A. W. & DOLIGALSKI, T. L. 1987 The impact of a vortex ring on a wall. *J. Fluid Mech.* **181**, 99–140.